PAPER • OPEN ACCESS

The surprising persistence of time-dependent quantum entanglement

New Journal of Physics
The open access journal at the forefront of physics

Deutsche Physikalische Gesellschaft DPG
IOP Institute of Physics

Published in partnership with: Deutsche Physikalische Gesellschaft and the Institute of Physics

OPEN ACCESS

RECEIVED
1 June 2022

REVISED
29 September 2022

ACCEPTED FOR PUBLICATION
5 October 2022

PUBLISHED
31 October 2022

PAPER

The surprising persistence of time-dependent quantum entanglement

Paul Kinsler*, Martin W McCall, Rupert F Oulton and Alex S Clark

Department of Physics, Imperial College London, London SW7 2AZ, United Kingdom
* Author to whom any correspondence should be addressed.

E-mail: Dr.Paul.Kinsler@physics.org

Keywords: quantum, entanglement, nonlinear, interferometer

Abstract

The mismatch between elegant theoretical models and the detailed experimental reality is particularly pronounced in quantum nonlinear interferometry (QNI). In stark contrast to theory, experiments contain pump beams that start in impure states and that are depleted, quantum noise that affects—and drives—any otherwise gradual build up of the signal and idler fields, and nonlinear materials that are far from ideal and have a complicated time-dependent dispersive response. Notably, we would normally expect group velocity mismatches to destroy any possibility of measurable or visible entanglement, even though it remains intact—the mismatches change the relative timings of induced signal–idler entanglements, thus generating 'which path' information. Using an approach based on the positive-P representation, which is ideally suited to such problems, we are able to keep detailed track of the time-domain entanglement crucial for QNI. This allows us to show that entanglement can be—and is—recoverable despite the obscuring effects of real-world complications; and that recovery is attributable to an implicit time-averaging present in the detection process.

1. Introduction

Quantum entanglement [1] is important because it plays a key role in a range of quantum devices, notably in induced coherence [2–4] based quantum imaging/QNI schemes [5–12]; and in the time domain is a subject of wide-ranging and active study [13–17]. However, the complicating effects of material dispersion in the entanglement-generating nonlinear medium, or during subsequent propagation, are typically not considered [18–20]. This has wider relevance, not only for quantum interference in general, but also e.g. in quantum data transmission [21–23] and quantum nonlinear interferometry (QNI). We demonstrate how and why, despite the complete de-synchronization of entangled fields caused by material dispersion, a slow detection process can perform an unexpected 'entanglement recovery', so that time resolved QNI can, after all, succeed.

Our testbed for examining the limitations on time-resolved quantum measurements is a pulsed QNI system where time dependence is relevant for all field interactions, in particular with the material dispersion (i.e. group velocity, and group velocity dispersion (GVD)) present alongside the entanglement-generating nonlinearity. In ghost imaging, for example, one can imagine a clear separation between standard (spatial) schemes [24, 25] and temporal schemes [26, 27], but if material dispersion was present during propagation, such simplicity would be disrupted. To address such intrinsic complications requires a shift in both theoretical methods and mindset; a description can no longer rely on using only a small number of possible states (typically Fock states), and judgements based on path indistinguishability or phase shifts. Instead, a set of time dependent states is required, and consequently it is not path lengths but relative timings that matter.

How fields propagate and are transported through a QNI system is shown on figure 1; the layout is very similar to that of Kolobov *et al* [28]. The key feature of the nonlinearity is that it produces correlated signal and idler photon pairs from an incoming pump field; this is often achieved using a $\chi^{(2)}$ interaction, but here

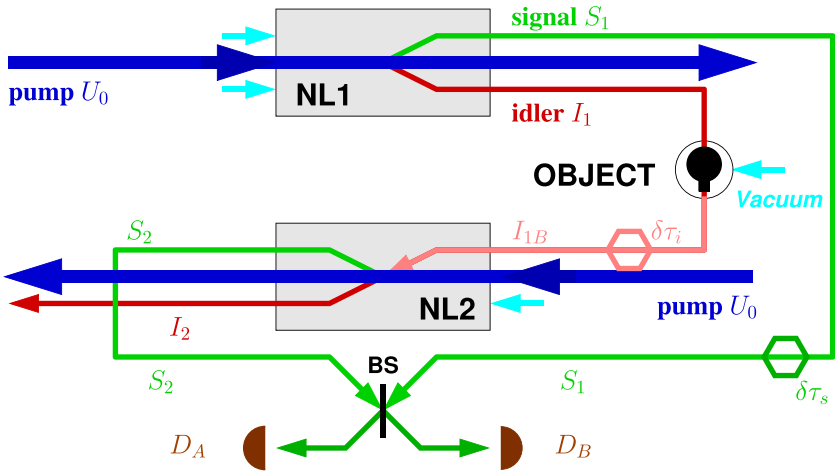

Figure 1. A representation of the QNI scheme (e.g. [28]). The two identical pump fields are in blue, signal fields in green, and idler in red; here the FWM process combines two pump photons to create a signal–idler pair. The resulting signal fields then interfere at the BS and detected at D_A and D_B. In an Imperial experiment [29], the nonlinear stages (NL1 and NL2) take place in opposite directions through the same length of fibre.

we use a degenerate-pump four wave mixing (FWM) (see e.g. [29]). A pump field enters the first nonlinear stage (NL1) and generates entangled signal and idler fields; and while the signal is diverted to the final beamsplitter (BS), the idler instead interacts with the to-be-imaged object, and then serves as a co-input, with a copy of the original pump field, to the second nonlinear stage (NL2). The signal field departing NL2 is thus influenced by an idler field entangled with the first signal field, and this information is extracted by interference at the output BS, before photon detection. Although here we test for entanglement using a QNI, an alternative would be to use a two-mode entanglement criterion [30].

The nonlinear propagation model in our simulations is a well-established one derived originally for the prediction of squeezing generation in optical fibres [31–35], has also been used to model multi-field parametric processes [36], and here centres primarily on multi-field nonlinear propagation through a dispersive material. It also includes stages representing setting up the initial conditions, interaction with an object to be imaged, and mixing at a BS at the interferometer output. In this work we use an established off-diagonal coherent state basis positive-P approach [37–39], that enables both group velocity and dispersion to be easily implemented in a numerical scheme [31]; crucially, its off-diagonal nature allows a complete representation of the full quantum mechanical density matrix of the system, and of its dynamics.

2. Propagation, nonlinearity and dispersion

In comparison to other models used to describe nonlinear interferometry, ours includes more features. Existing approaches tend to be simple and rather abstract, relying on Fock states, CW or monochromatic fields, and idealized materials (e.g. purely nonlinear materials). In contrast, real systems have bandwidth, are time dependent, use pulses, and rely on imperfect materials with dispersive properties and substructure (e.g. periodic poling). Thus existing simple models are not sufficient to describe the physics present in nonlinear interferometers, and this necessarily affects the depth of our understanding. Here we include nonlinearity, dispersion, and propagation on an equal footing, providing a good coverage of the unavoidable and significant physical processes present in QNI applications.

Our description treats each optical pump pulse as a set of time-dependent quasi-conjugate pump field amplitudes $\alpha_u(t)$, $\alpha_u^\dagger(t)$, which are only complex-conjugate on average; and we do likewise for the signal $\alpha_s(t)$, $\alpha_s^\dagger(t)$, and idler $\alpha_i(t)$, $\alpha_i^\dagger(t)$ pulses. There is also a set of independent time-dependent noise increments $\{\mathrm{d}W_a(t)\}$. In simulation, time is discretized and labels a set of finely divided, *sub-pulse length* modes [40, 41] where each field is held as an array of sequential 'time-bins' (or 'temporal modes') at $t \in \{t_j\}$, each of which contains pairs of complex field amplitudes; these interact and evolve as the fields propagate step-by-step through space. Since these time-bins have a simulation-specific duration, field averages such as $\langle \alpha_s^\dagger \alpha_s \rangle$ represent intensity (in photons per second), not photon number, and normalizations and parameter scalings reflect this.

This field information is held along with fixed parameters for the nonlinear coupling κ, losses γ_m, and dispersive properties $D_m(\omega)$, where the field subscripts, as above, are $m \in \{u, s, i\}$. Since this is a stochastic

technique, very many independent copies of the evolution need to be run (for the simulations here, typically in the range 10^5 to 10^7), and the necessary ensemble averages taken.

This propagation model is very close to previous ones (e.g. [31, 34, 36]), but here we have three co-propagating fields and a different nonlinear interaction; namely one for the degenerate FWM process with only resonant wave mixing terms where $2\omega_u = \omega_s + \omega_i$. Since self-phase modulation (SPM) terms are not significant in the low-power regime (see e.g. [29]), the interaction Hamiltonian we need here is simply

$$\hat{H}_{\mathrm{fwm}} = \imath\hbar\chi\hat{a}_u^{\dagger 2}\hat{a}_s\hat{a}_i - \imath\hbar\chi^*\hat{a}_u^2\hat{a}_s^\dagger\hat{a}_i^\dagger. \tag{1}$$

This interaction term results in propagation equations which are best expressed in the incremental form suited to such stochastic differential equations (SDEs) [37]. In an appropriate co-moving frame, including loss along with nonlinear effects [34], but suppressing the time argument common to all fields $\alpha_m, \alpha_m^\dagger$ and quantum noise increments $\mathrm{d}W_a$, we have (see appendix A)

$$\mathrm{d}\alpha_s = \left[-\gamma_s\alpha_s + \chi^*\alpha_u\alpha_u\alpha_i^\dagger\right]\mathrm{d}z + \left\{(2\chi)^{1/2}\alpha_u\right\}\mathrm{d}W_1, \tag{2}$$

$$\mathrm{d}\alpha_s^\dagger = \left[-\gamma_s\alpha_s^\dagger + \chi\alpha_u^\dagger\alpha_u^\dagger\alpha_i\right]\mathrm{d}z + \left\{(2\chi^*)^{1/2}\alpha_u^\dagger\right\}\mathrm{d}W_2, \tag{3}$$

$$\mathrm{d}\alpha_i = \left[-\gamma_i\alpha_i + \chi^*\alpha_u\alpha_u\alpha_s^\dagger\right]\mathrm{d}z + \left\{(2\chi)^{1/2}\alpha_u\right\}\mathrm{d}W_1, \tag{4}$$

$$\mathrm{d}\alpha_i^\dagger = \left[-\gamma_i\alpha_i^\dagger + \chi\alpha_u^\dagger\alpha_u^\dagger\alpha_s\right]\mathrm{d}z + \left\{(2\chi^*)^{1/2}\alpha_u^\dagger\right\}\mathrm{d}W_2, \tag{5}$$

$$\mathrm{d}\alpha_u = \left[-\gamma_u\alpha_u - 2\chi\alpha_u^\dagger\alpha_s\alpha_i\right]\mathrm{d}z + \imath\{2\chi\alpha_s\alpha_i\}^{1/2}\mathrm{d}W_3, \tag{6}$$

$$\mathrm{d}\alpha_u^\dagger = \left[-\gamma_u\alpha_u^\dagger - 2\chi^*\alpha_u\alpha_s^\dagger\alpha_i^\dagger\right]\mathrm{d}z + \imath\left\{2\chi^*\alpha_s^\dagger\alpha_i^\dagger\right\}^{1/2}\mathrm{d}W_4. \tag{7}$$

These equations are used to update each time-bin in the temporal profile of the fields as that profile propagates (steps) forward in space, i.e. propagates along the optical fibre. Deterministic evolution terms are in square brackets $[\cdots]$, and prefactors for the stochastic (noisy) terms are in braces $\{\cdots\}$. The noises are uncorrelated, with $\delta_{ab} = \langle \mathrm{d}W_a(t)\mathrm{d}W_b(t)\rangle$. Note that a classical model of the same process (or even a semi-classical model, see e.g. [42–44]) would have only three equations and *no* noise terms.

Here we see that there are both coherent interactions between the three fields, and correlated nonlinear quantum noise terms. The noise increment $\mathrm{d}W_1$ drives both α_s and α_i, while $\mathrm{d}W_2$ drives $\alpha_s^\dagger$ and $\alpha_i^\dagger$, ensuring the pairs are correlated but *not* complex conjugate. This freedom allows us to represent entanglement [1] as classical statistical correlations between complex field amplitudes which are capable of reproducing the off-diagonal elements of the density matrix—i.e. they can represent all the necessary quantum properties [37]. This is possible because each field is represented by two independent amplitudes α_m and $\alpha_m^\dagger$; and although they are complex conjugate on average, i.e. $\langle\alpha_m\rangle = \langle\alpha_m^\dagger\rangle^*$, in any given trajectory making up part of the large ensemble, they need not be. By looking at the SDE's for the nonlinearity (2)–(7), we can see that the non-daggered and the daggered amplitudes are driven by *different* noises. Thus both the mean photon numbers $\langle\alpha_s^\dagger\alpha_s\rangle$ and $\langle\alpha_i^\dagger\alpha_i\rangle$ could even remain nearly zero even while a significant quantum statistical correlation (i.e. entanglement) is being created between the signal and idler fields; i.e. between α_s and α_i, and between $\alpha_s^\dagger$ and $\alpha_i^\dagger$.

Material dispersion is the other key feature, and we interleave it with the nonlinearity in a split-step scheme (see e.g. Carter *et al* [31, 34]), using linear phase shifts in the spectral domain for group velocity v_g, and quadratic shifts for GVD. This process, with the exception of the need to apply it to quasi-conjugate field profiles $\alpha_m^\dagger(t)$ as well as the $\alpha_m(t)$ profiles, is essentially identical to that used to apply dispersion in classical pulse propagation scenarios.

3. Material parameters and objects

The material and input parameters in the simulations are chosen to ensure the time-dependent nature of the entanglement will be most exposed to the disruptive effects of material dispersion, which allows us to demonstrate our findings most clearly. Nevertheless, to remain relevant to at least one experimental regime, we choose our parameters to be compatible with fiber-based photon pair sources based on spontaneous FWM [29], which use about 100 cm of Thorlabs PM780-HP fibre (see table 1). For the simulation, we convert parameters into units based on metres (m), picoseconds (ps), and field excitation amplitudes are referenced back to photon numbers per picosecond. However, note that any particular parameter's numerical value is less important than the relationships between it and other parameter values. A crucial

Table 1. Material parameters used in the simulations, based on the experimental setup of [29]. Since the fibre is weakly guiding, these are based on those for bulk silica. The nonlinearity in SI units is $n_2 = 3 \times 10^{-20}$ m^2 W^{-1}, the loss is $\gamma = 0.004$ m, and Δv_g is the difference in group velocity between the fields as compared to the pump value. In simulation units, the PM780-HP's stated transverse field mode area of about 25 μm^2 and the pump photon energy of 25×10^{-20} J, means that the rescaled nonlinearity is $n_2'' = 0.3 \times 10^{-15}$ per photon-picosecond. In a time-bin T ps long, the pump photon has a power $\sim(0.25/T)$ μW, so that a power of 100 W corresponds to a flux of 4×10^8 photons ps^{-1}. Estimates for signal and idler fields are similar. Note that the pump powers used in the simulations are increased to enable good simulation statistics (see appendix B).

Field	Wavelength (nm)	Frequency (THz)	Δv_g (ps m^{-1})	Dispersion d_2 (ps^2 km^{-1})
Pump	768	390.5	0	0.589
Signal	700	428.0	−100	0.489
Idler	850	353.0	+83	0.721

step for our demonstration here is to consider pulsed operation on a picosecond scale, where the group velocity mismatches become significant during propagation through the optical fibre.

Since the effect of group velocity mismatches and GVD turns localised entanglements into temporally distributed ones in our simulations we see a fan of signal amplitudes that spreads out behind the pump pulse, while a fan of idler amplitudes spreads out before. Thus, crucially, the signal–idler entanglement is not only distributed over a range of times, it is also between *different* times; i.e. it is a multi-time correlation. For best imaging visibility, this requires careful synchronisation at NL2, where the first-generated part of the idler in NL2 should be coincident with the pump pulse as it enters.

Objects placed in the idler beam leaving the NL1 stage disrupt its entanglement with the first signal beam, and that disruption changes the second signal beam it helps create. As a result, the interference of the two signal beams at the BS enable the object's presence or properties to be inferred by comparing enable the numbers of detected photons at the interferometer output ports. However, in non-imaging contexts, we could view such objects as representatives of further disruptive unwanted real-world effects: loss, phase shifts through optical elements, or extraneous couplings.

In this work we primarily consider passive objects that impart either (i) a phase modulation $\Delta\phi$ of the idler field, or have (ii) a reflectivity r that reduces the idler amplitudes as they pass (as in [28]); so $r = 1$ removes all entanglement.

We also consider (iii) imaging of dynamic objects, a key feature of interest since an object's time dependence will affect visibility, just as timing, group velocity, and GVD do. Our linearly coupled dynamic objects with amplitudes $\beta(t), \beta^\dagger(t)$ respond to the incident pulse profile $\alpha_m(t), \alpha_m^\dagger(t)$ at the position z specific to the object; and a field–object interaction strength η. At the object we set the initial conditions at t_o so that $\beta(t_o) = \beta_o$ and $\beta^\dagger(t_o) = \beta_o^*$, and then *time* integrate $\beta(t), \beta^\dagger(t)$ using

$$\mathrm{d}\beta(t) = \left[-\gamma_o\beta(t) + \eta^*\alpha_m(t)\right]\mathrm{d}t, \tag{8}$$

$$\mathrm{d}\beta^\dagger(t) = \left[-\gamma_o\beta^\dagger(t) + \eta\ \alpha_m^\dagger(t)\right]\mathrm{d}t. \tag{9}$$

Now that the incident field $\alpha_m, \alpha_m^\dagger$ has excited the dynamic object, this excitation acts back on the field and modifies it. We therefore then update $\alpha(t), \alpha^\dagger(t)$ according to the same linear interaction but here integrated forward in *space*, using

$$\mathrm{d}\alpha_m(t) = -\frac{1}{2}\eta\ \beta(t)\mathrm{d}z; \qquad \mathrm{d}\alpha_m^\dagger(t) = -\frac{1}{2}\eta^*\beta^\dagger(t)\mathrm{d}z, \tag{10}$$

and keeping the SDE notation for consistency. Note that this could be extended to allow for nonlinear couplings or dynamics with the object, or to even use (e.g.) a two-level-atom or Raman models (see e.g. a classical counterpart [46]).

4. Simulation & statistics

Our simulations, in common with all of their type [31–34], calculate and report ensemble averages of field amplitudes, intensities, or correlations. To achieve this we run an ensemble made up of many thousands (or millions) of copies of the system, each with the same initial conditions and parameters, but each based on a different and independent sequence of random quantum noise increments. Fortunately, due to the nature of the representation, linear elements such as BSs, our simple objects, or the detection process, do not introduce extra noise. As a result, the only noise that is present is that from the nonlinear stages

(i.e. as given in (2)–(7)). Nevertheless, because the simulations can only attempt a sample of the possible evolutions, the results are necessarily affected by the unavoidable uncertainties introduced by a finite ensemble, and this statistical sampling error can only be reduced by increasing the ensemble size.

Further, it has long been known that getting good simulation statistics with the fully quantum mechanical positive-P representation can be challenging [34]. This means that it is very common to resort to the much simpler, but approximate, truncated Wigner representation [39] in simulations. In contrast to the positive-P, the truncated Wigner representation is essentially a semi-classical hidden variable model that represents the quantum uncertainty as simple statistical fluctuations in the field amplitudes [42, 43]. This halves the number of equations required by the simulation (needing only a single complex α rather than the double α and $\alpha^\dagger$), reducing the state space, and resulting in an effective and sufficiently accurate method when e.g. studying quadrature squeezing [47], and its generation using optical pulses in nonlinear materials [31, 32, 34, 35].

However, in this work, here we want to ensure an accurate representation of the quantum effects, and so we stay with the full positive-P model (cf the case of quantum tunnelling [42, 43] and nonlinearity and the quantum vacuum [44]). Since the subtler effects of quantum entanglement are addressed here, rather than the simpler quadrature moments, a truncated Wigner representation would not suffice, since it imposes an unavoidable linkage between correlations and photon number. This leaves us requiring the use of a full positive-P description and concomitant extremely large computational demands. This is especially problematic since we may need to resolve very low average photon numbers inside an extremely noisy background.

We address this using a hybrid strategy which allows us to use just *one* very high ensemble number M_B simulation to get a good estimate of the background for some particular case, and then adjusting this using two more simulations with lower ensemble numbers M_R but perfectly matched random noise generation. We call the M_B simulation the 'background', and the other two the 'reference' and 'target' simulations. The reference simulation has identical parameters to the background simulations, and the target simulation has the parameters corresponding to the particular result we are interested in. The difference between the reference and target simulations only depends on the differences between the system parameters, with only 'second-order' noise effects—resulting from how the noise influences propagation differently, and not from different random number sequences.

When trying to evaluate a photon number n for some chosen target parameters, we proceed as follows, using the usual notation where a statistical average is denoted $\langle n\rangle$, but additionally adding a subscript to denote the ensemble size, with ∞ to denote the ideal infinite-ensemble case. Each trajectory in the background or reference ensembles returns a value n'_j, and each in the target ensemble returns n_j.

Thus for n' we can have either a low sampling error, or a larger sampling error, as follows

$$\langle n'\rangle_\infty \simeq \langle n'\rangle_{M_B} = \frac{1}{M_B}\sum_{j=1}^{M_B} n'_j \tag{11}$$

$$\approx \langle n'\rangle_{M_R} = \frac{1}{M_R}\sum_{j=1}^{M_R} n'_j, \tag{12}$$

with the sampling error reducing for each as M_B and M_R are increased; thus for large enough M values we have

$$\langle n'\rangle_{M_B} \approx \langle n'\rangle_{M_R} \tag{13}$$

$$\text{i.e.}\quad \langle n'\rangle_{M_B} - \langle n'\rangle_{M_R} \approx 0, \tag{14}$$

but noting that the noise-sampling error in this approximate equality (14) is dominated by the larger variation in the smaller reference ensemble.

Similarly, for n we have

$$\langle n\rangle_\infty \approx \langle n\rangle_{M_R} = \frac{1}{M_R}\sum_{j=1}^{M_R} n_j. \tag{15}$$

Since the lhs of (14) should average to zero, we can now write

$$\langle n\rangle_\infty = \langle n\rangle_\infty - \langle n'\rangle_\infty + \langle n'\rangle_\infty \tag{16}$$

$$\approx \langle n\rangle_{M_R} - \langle n'\rangle_{M_R} - \langle n'\rangle_{M_B}, \tag{17}$$

which, given its dependence on both $\langle n\rangle_{M_R}$ and $\langle n'\rangle_{M_R}$, would at first appear to suffer a larger sampling error based on the smaller M_R, not a small sampling error based on the large M_B.

However, the key point is that since we have *exactly* matched the simulation noise values between the reference simulations of n'_j and target simulations of n_j then their difference is due to differences of the trajectory dynamics between the two simulations, and is only weakly dependent on the specific noise values. Since this cancels out the bulk of the sampling error due to the noise in these smaller-ensemble simulations, we can now write

$$\langle n\rangle_{\infty} \simeq \langle n\rangle_{M_R} - \langle n'\rangle_{M_R} - \langle n'\rangle_{M_B}, \tag{18}$$

where now it is the sampling error from the *background* ensemble that dominates.

Thus for any parameter set, we only need to do one large ensemble M_B background simulation, one smaller ensemble M_R reference simulation otherwise *identical* to the background one, and then then many small M_R target simulations which do have a parameter variation compared to the background simulation. Background parameters were of systems with perfectly transparent objects, and our target simulations varied only the object properties.

To look forward to our main results, we typically did background simulations with M_B sizes from $\sim 10^6$ (for figures 4(a) and (d)) to $\sim 16\times 10^6$ (for figures 4(c) and (f) and 5), and reference and target simulations with $M_R = 128\times 10^3$. In the most extreme case, this gave us a factor of 125 improvement in effective simulation speed, as well as the crucial decrease in statistical error. Every single results curve shown on figure 5 – i.e. for each different idler offset, each different object phase or reflectivity, and each different object coupling strength—could be based on a *single* high-M_B background simulation. This enabled a large and very necessary reduction in total simulation time, since each extra result only needed a simulation with the much smaller M_R samples. While it may be possible to vary other parameters, or perhaps even several parameters at once, this will induce a greater divergence between propagation in the reference and target systems, and so affect the extent of any improvement.

5. Entanglement and visibility

The photon number rate as measured at the detectors is taken to be the ensemble-averaged photon number of the relevant field at that point. An important quantity is the *visibility* of the entanglement, and the amount of entanglement between the interferometer's two signal fields is indicated by the difference in the two detector counts at the outputs of the interferometer. The visibility is therefore the difference of the detector counts ('signal') divided by the sum of the detector counts ('background'); i.e.

$$\mathcal{V}_{AB} = \frac{|n_A - n_B|}{(n_A + n_B)}. \tag{19}$$

This visibility definition, while key to measuring the performance of the interferometer, can become problematic for the pulsed situations we cover later in this work. However, note that this $\mathcal{V}_{AB}$ is not strictly an entanglement witness [30, 45].

For a time-dependent case where the detected fields are pulses, there will be very low average amplitudes in the pulse wings. This means that random noise contributions in the wings can easily dominate the calculated visibility, and obscure and distract from its true value. To suppress such sampling artefacts in pulsed cases, we add to the background $n_A + n_B$ an offset of 0.05% of its maximum value, i.e. that at the pulse centre.

The simplest detection model is to assume that each simulation time-bin gives rise to its own independent detections. However, since the time-bin widths are set by the needs of the simulation, they are unlikely to correspond to any property of an actual detector. To address this, below we introduce a simple time-averaging detector model, although a more sophisticated approach could to adapt the time-dependent object model discussed above.

5.1. CW simulations

We test the basics of the simulations with a simple CW-equivalent parameter set with no group velocity or GVD effects. This requires just a single extra one time-bin simulation per parameter change, so it is easy to look at how the visibility varies with object phase-shifts and object reflectivities. Here, correlations between the first signal's time-bins and the second signal's ones will always be synchronised, maximizing the visibility. For sufficiently low signal–idler generation efficiencies, we should see equal photon number intensities in the signal's field-modes, but distinct photon number intensities after the BS, i.e. at the two detectors; this is clearly shown on figure 2.

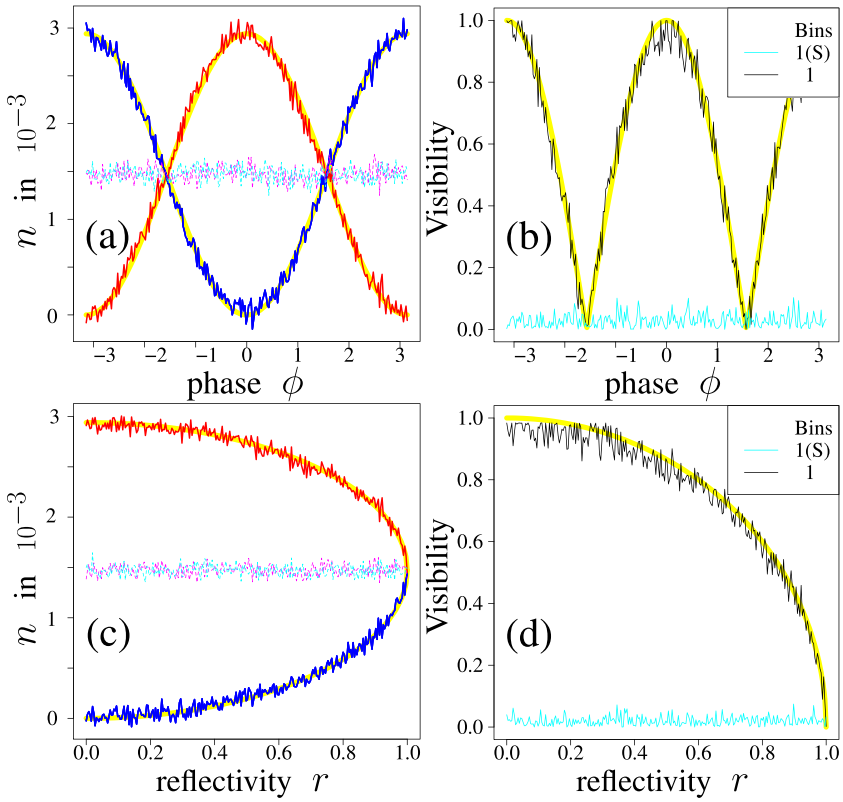

Figure 2. Entanglement visibility versus a specified phase shift (top) and reflectivity (bottom) caused by an imaged object. (a) and (c) Photon counts at detectors D_A, D_B (in red and blue), compared to photon numbers in the pre-BS signal fields S_1, S_2 (dashed, in cyan and magenta). (b) and (d) Visibility based on detector measurements (black) compared against one calculated from signal fields (cyan). On (c) and (d), the $r = 1$ end result gives the case of a blocking object, i.e. no entanglement. Statistical noise can be reduced by increasing the ensemble sizes from 256 k, but are retained as-is to emphasise the necessity of the ensemble averaging. The results match the theoretical fits shown in the background as thick yellow lines.

6. Detection and time averaging

Time averaging is a crucial part of any detection model used here, since real detectors are very slow (typically $\gg$ 100 ps) when compared to the temporal resolution of our simulations ($\sim$ps). Although more sophisticated models can easily be imagined, here we simply sum the time-binned amplitudes of each field over some chosen m-bin detector response time, before ensemble averaging to get the detected photons. This assumes that the detector is responding to the cumulative effects of the impinging electric field amplitudes, before eventually reporting its photon number count; it is *not* just summing up a sequence of rapidly taken photon counts. Thus we have

$$\bar{n}_D = \langle \bar{\alpha}^\dagger \bar{\alpha} \rangle, \quad \text{with} \quad \bar{\alpha}^{(\dagger)} = (\frac{1}{m})^{1/2} \sum_{i=1}^{m} \alpha^{(\dagger)}(t_i). \tag{20}$$

Crucially, this averaging process in the detector helps expose amplitude correlations in the between time-bins that have become offset due to dispersion mismatches (see appendix C for a toy model of this). Note that this summation is essentially the same as the process for combining multiple short time bins into a longer one; just as we need to do in numerical convergence checks.

With this ability to consider the time-averaging properties of detectors in place, we can now use our simulations to see both (a) the deleterious effect of dispersion on entanglement visibility, and (b) the ability of detector averaging to recover it. Although it seems unlikely, given the complicated and gradual effects of nonlinearity and dispersion, that this will grant perfect entanglement recovery, we now test the interplay of group velocity offsets and dispersion with this detector time-averaging in place.

6.1. Dispersion vs entanglement visibility

Here we consider a quasi-CW case where the pump, signal, and idler fields are all allowed to be time-dependent, but the input pump field is not a pulse but instead has a constant amplitude. Roughly speaking, therefore, each triplet of (pump, signal, idler) time-bins in the simulation therefore generates

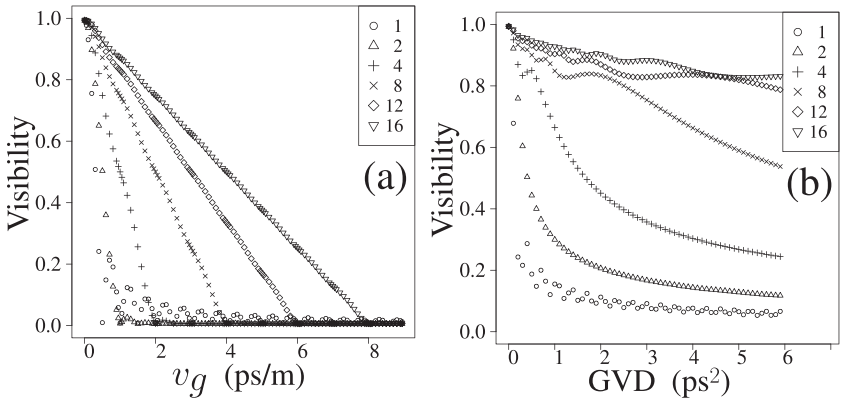

Figure 3. Detectable entanglement is obscured by material dispersion, even though the entanglement itself remains: the no-object case, as group velocity (v_g) and GVD mismatches increase, for 100 cm propagation with standard parameters, and comparing detection time-averaging intervals. Here the mismatch is applied to the signal field S_1, so that a v_g mismatch causes a timing offset $\delta\tau_s$ at the BS. Circles (○) are 'fast detector' un-averaged results, other symbols show the number of adjacent 0.5 ps time-bins averaged. For v_g mismatches (a), the regular residual bumps in ○ are a discretization artefact, and can be further suppressed by increasing the time resolution. The complicated effect of GVD mismatches (b) leads to smooth variations as different contributions de-phase or rephase.

their own entanglement; but as the fields propagate through the nonlinear material, dispersion takes its effect. The v_g or GVD mismatches between fields causes that entanglement to migrate and/or diffuse between time-bins. This means that even though the entanglement is always fully present, and does not reduce, its *visibility* is reduced, and is reduced more for greater mismatches, as can be seen on figure 3. However, figure 3 also shows that visibility can be recovered using longer averaging intervals; at least up to a (v_g) cut-off when the time difference exceeds the averaging windows.

Note that there *is* a regime in which long-time detector averaging might instead lead to reduced entanglement visibility. This is the case where the input pump pulses are longer than their coherence time, i.e. that they are comparable to an ensemble of dissimilar, but perfectly coherent, shorter pulses with randomly staggered arrival times. In such a case, if detector averaging is also longer than the coherence time, the entanglement visibility might be obscured under the additional noise and variation.

7. Pulsed SFWM simulations

Having demonstrated the visibility-reducing effect of dispersion, and the compensating nature of detection averaging for instructive but artificial material parameters, we now proceed to consider more realistic situation. Here we standardise on an input 40 ps pump pulse and a 512 ps window divided into 2 ps bins. Simulation pulse intensities were chosen as low as practicable, given the constraints of computation time and the requirement for good simulation statistics. Further, the pump–idler pulses were ideally synchronised as they entered the NL2 stage. However, the signal fields are also mis-timed at the output BS by $\delta\tau_s = 20$ ps (i.e. ten time bins). This not only mimics imperfect experimental setup, it is also useful in providing an example where the detector averaging has more to recover. We also used the technique, described in section 4, to reduce the effect of sampling error—something which would otherwise make useful positive-P simulations computationally prohibitive or problematic, since statistical fluctuations due to poor sampling artificially increase the computed visibility.

In figures 4(a)–(f) we show how detected photon numbers and visibilities vary for no interposed in-interferometer object. To increase the generality of our results, we not only use our standard material parameters (c) and (f), but also show some for artificially reduced group velocity offsets (a), (d) and (b), (e). This range of material parameter values emphasises the significant effect of group velocity offsets. The displacement to negative t of the visibility peak is a result of the group velocity walk-off of the signal field.

We see that the detected photon rates n decrease at larger group velocity mismatches—this is due to the increased spreading of the generated fields, and hence less effective nonlinear generation. Despite the decrease in detected n, we see that the reduction in detector-averaged entanglement visibility is relatively minor; while in stark contrast, the drop in *un-averaged* visibility is significant. Thus we see that sufficiently long averaging interval allows us to recover most of the maximum possible visibility, albeit not all; and as we would expect the averaging also helps reduce the significant statistical variation visible on the un-averaged data. Thus figure 4 shows that group velocity mismatches are not as problematic as they might

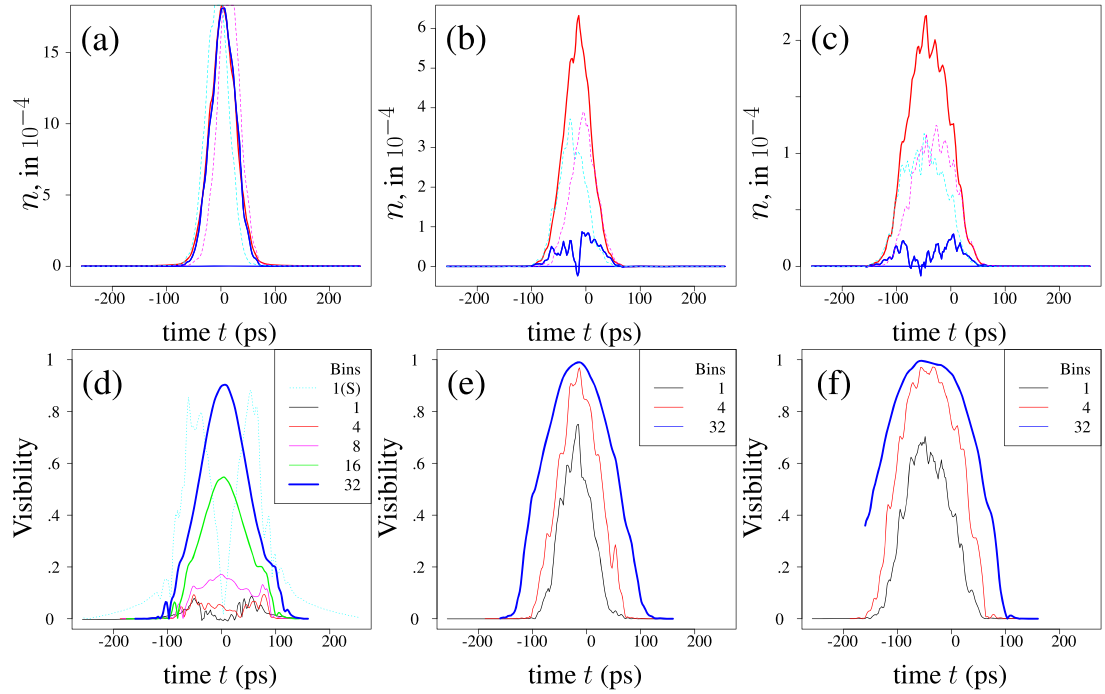

Figure 4. Pulsed simulations with no object ($r = 0$) and artificially scaled ((a) and (d) 10%, (b) and (e) 50%) and true (c) and (f) group velocity offsets. (a), (b) and (c) Detected photon numbers per 2 ps, n_A, n_B (red and blue); dotted lines are n_{s1}, n_{s2} for the pre-BS signal fields; note the change in vertical axis scale. (d), (e) and (f) Detected entanglement visibilities for different time averaging, at 2 ps per bin. The 1(S) curve on (d) is a (false) visibility based on an assumed detection of the pre-BS signal pulses, and is non-zero only because of their arrival-time mismatch.

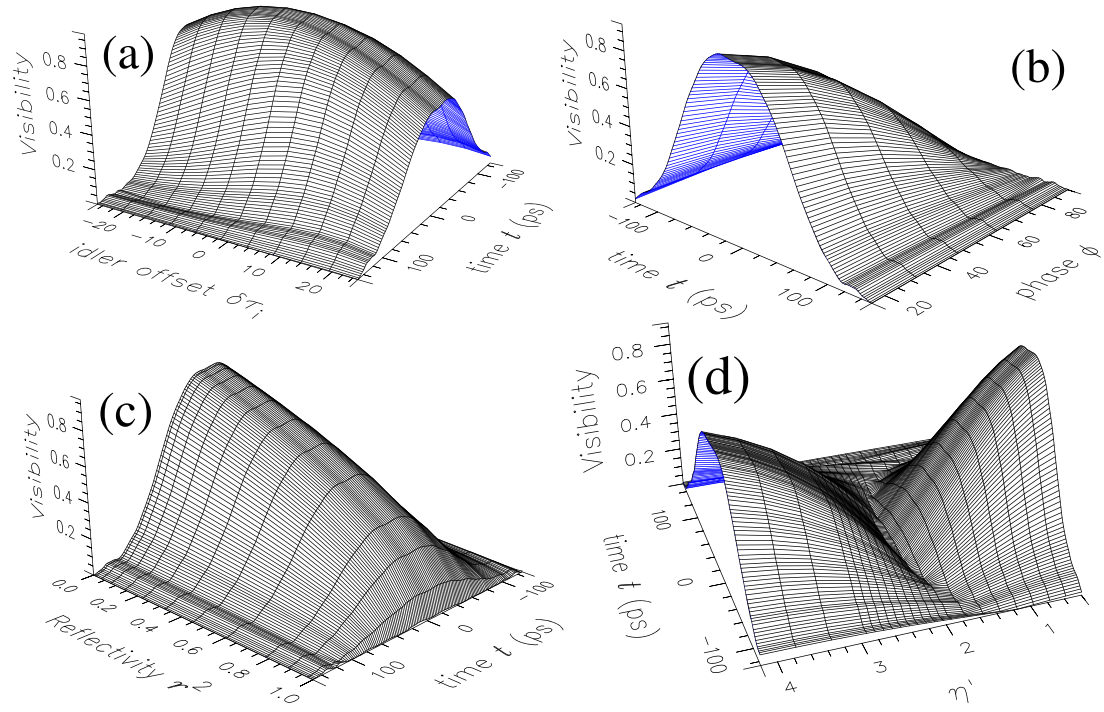

Figure 5. Time-dependent entanglement visibilities for pulsed simulations with 32 bin (64 ps) averaging and a 40 ps mistiming at the output BS. In (a) we see how the visibility profile changes if the idler synchronisation $\delta\tau_i$ (in ps) differs from the ideal value. Other frames show the effects of varying object properties, i.e. (b) phase (in degrees), (c) reflectivity, and (d) interaction with a dynamic object as per (8)–(10).

at first appear, since the generated entanglements, however scrambled they might be by the gradual nonlinear generation and significantly dispersive propagation, *can* be recovered to a significant extent by time-averaging at the detector.

In figure 4 the simulations ensured the idler pulse arrived at the NL2 stage in correct synchronization with the pump pulse. We can see on figure 5(a) that mis-timing the idler pulse arrival results in a gradual fall off in averaged visibility. This is due to a combination of the pump pulse length (40 ps), the averaging time (64 ps), and the group velocity spreading (∼80 ps); although we expect this behavior to be typical, and not specific to these exact parameters.

On figures 5(b) and (c), we introduce passive objects into the simulations that cause either (b) an idler phase shift, or have (c) a reflectivity that reduces the idler amplitude. In these, and in broad agreement with the CW case trends shown in figure 2, we see a fall-off of the time-dependent entanglement visibility with object phase depth ϕ and object reflectivity r.

Dynamic objects further emphasise the potential role of time-dependence. Figure 5(d) shows recovered entanglement visibility values for a range of interaction strengths η'. At low η', idler field excitations are coupled into the object but not out again, leading to reduced visibility. However, as the η' increases even further, those excitations can also start being coupled back out, leading to a partial recovery. This non-trivial behaviour suggests the possibility of interesting trade-offs between parameter regimes when considering the imaging of dynamic objects.

8. Conclusion

We have shown how the time-averaging process inherent in slow detector response times enables recovery of the entanglement necessary QNI. Unexpectedly, this remains true even when significant confounding effects such as group velocity differences, dispersion, mis-timing of pulse arrivals, or objects interposed in the idler beam are allowed for. But although such a 'detector averaging' argument might sound plausible enough for very simple scenarios, for descriptions approaching any real-world complexity obtaining any straightforward theoretical confirmation is unlikely. Accordingly, here we have used numerical simulations to test both simple CW and complicated pulsed scenarios and can confirm the important role of detector time averaging. Although one could consider adding additional detail to our model, such as other experimental noise sources, by including nonlinearity, dispersion, and propagation effects we have nevertheless already included all the key physical processes.

In particular, group velocity mismatches play a critical role, seeing as they can rapidly de-synchronise mutually entangled time-slices of the light field. As a result the essential lesson to draw from this work is clearly visible on figure 3; i.e. that entanglement visibility can be recovered if the detection averaging timescale is greater than the group velocity walk-off (see figure 3(a)), or greater than the timescale of the dispersively-induced dephasing (see figure 3(b)). However, as the later results show (see figures 4 and 5), in more realistic systems the interplay of these effects can give rise to more complicated dependencies, although the trend—more averaging implies better visibility—remains clear. In contrast to visibilities, which are a ratio, nonlinear generation efficiencies suffer penalties from the effect of material dispersion regardless of averaging.

Finally, here we have also introduced a linearly coupled, dynamic object model to act as a starting point for more modelling of more sophisticated interactions; a feature likely to be important in systems relying on short pulses, resonant behaviour, and time-domain entanglement.

Acknowledgments

Support from the UK National Quantum Hub for Imaging (QUANTIC, EP/T00097X/1).

Data availability statement

The data that support the findings of this study are available upon reasonable request from the authors.

Appendix A. Evolution: from density matrix to SDEs

Since to our knowledge the positive-P Fokker–Planck equation for the degenerate-pump FWM interaction Hamiltonian are not currently in the literature, so we now summarize the derivation. This interaction Hamiltonian (1) gives a contribution to the density matrix evolution

$$\dot{\rho}_{\text{int}} = \frac{\imath}{\hbar}\left[\hat{H}_{\text{int}}, \rho\right]. \tag{21}$$

The expansion of the density matrix in terms of coherent states, albeit for just a single mode, is

$$\rho = \int \frac{|\alpha\rangle\langle\alpha^\dagger|}{\langle\alpha|\alpha^\dagger\rangle} P(\alpha,\alpha^\dagger;t)\mathrm{d}^2\alpha\,\mathrm{d}^2\alpha^\dagger. \tag{22}$$

Using the standard positive-P operator correspondences, we can convert the density matrix dynamics into a dynamics for the corresponding positive-P distribution function [37–39], which is a function of many complex coherent state amplitudes. The resulting Fokker–Planck equation for this $P(\ldots;\ t)$ is

$$\partial_t P(\ldots;t) = \mathscr{L}_{\mathrm{int}} P(\ldots;t). \tag{23}$$

The derivative operators defining this part of the dynamics for the positive-P distribution P is as follows. The first two lines result from the first commutator term $\hat{H}_{\mathrm{int}}\rho$, and the last two lines from $-\rho\hat{H}_{\mathrm{int}}$, are

$$\begin{aligned}\mathscr{L}_{\mathrm{int}} = &-\chi\left(\alpha_u^\dagger + \frac{\partial}{\partial\alpha_u}\right)^2\alpha_s\alpha_i \\ &+ \chi^*\alpha_u\alpha_u\left(\alpha_s^\dagger + \frac{\partial}{\partial\alpha_s}\right)\left(\alpha_i^\dagger + \frac{\partial}{\partial\alpha_i}\right) \\ &+ \chi\alpha_u^\dagger\alpha_u^\dagger\left(\alpha_s + \frac{\partial}{\partial\alpha_s^\dagger}\right)\left(\alpha_i + \frac{\partial}{\partial\alpha_i^\dagger}\right) \\ &- \chi^*\left(\alpha_u + \frac{\partial}{\partial\alpha_u^\dagger}\right)^2\alpha_s^\dagger\alpha_i^\dagger.\end{aligned} \tag{24}$$

Expanded we have,

$$\begin{aligned}&-\chi\left\{\alpha_u^\dagger\alpha_u^\dagger + \alpha_u^\dagger\frac{\partial}{\partial\alpha_u} + \frac{\partial}{\partial\alpha_u}\alpha_u^\dagger + \frac{\partial}{\partial\alpha_u}\frac{\partial}{\partial\alpha_u}\right\}\alpha_s\alpha_i \\ &+\chi^*\alpha_u\alpha_u\left\{\alpha_s^\dagger\alpha_i^\dagger + \alpha_s^\dagger\frac{\partial}{\partial\alpha_i} + \frac{\partial}{\partial\alpha_s}\alpha_i^\dagger + \frac{\partial}{\partial\alpha_s}\frac{\partial}{\partial\alpha_i}\right\} \\ &+\chi\alpha_u^\dagger\alpha_u^\dagger\left\{\alpha_s\alpha_i + \alpha_s\frac{\partial}{\partial\alpha_i^\dagger} + \frac{\partial}{\partial\alpha_s^\dagger}\alpha_i + \frac{\partial}{\partial\alpha_s^\dagger}\frac{\partial}{\partial\alpha_i^\dagger}\right\} \\ &-\chi^*\left\{\alpha_u\alpha_u + \frac{\partial}{\partial\alpha_u^\dagger}\alpha_u + \alpha_u\frac{\partial}{\partial\alpha_u^\dagger} + \frac{\partial}{\partial\alpha_u^\dagger}\frac{\partial}{\partial\alpha_u^\dagger}\right\}\alpha_s^\dagger\alpha_i^\dagger.\end{aligned} \tag{25}$$

Now all the terms without derivatives cancel, so that

$$\begin{aligned}&-\chi\left\{\alpha_u^\dagger\frac{\partial}{\partial\alpha_u} + \frac{\partial}{\partial\alpha_u}\alpha_u^\dagger + \frac{\partial}{\partial\alpha_u}\frac{\partial}{\partial\alpha_u}\right\}\alpha_s\alpha_i \\ &+\chi^*\alpha_u\alpha_u\left\{\alpha_s^\dagger\frac{\partial}{\partial\alpha_i} + \frac{\partial}{\partial\alpha_s}\alpha_i^\dagger + \frac{\partial}{\partial\alpha_s}\frac{\partial}{\partial\alpha_i}\right\} \\ &+\chi\alpha_u^\dagger\alpha_u^\dagger\left\{\alpha_s\frac{\partial}{\partial\alpha_i^\dagger} + \frac{\partial}{\partial\alpha_s^\dagger}\alpha_i + \frac{\partial}{\partial\alpha_s^\dagger}\frac{\partial}{\partial\alpha_i^\dagger}\right\} \\ &-\chi^*\left\{\frac{\partial}{\partial\alpha_u^\dagger}\alpha_u + \alpha_u\frac{\partial}{\partial\alpha_u^\dagger} + \frac{\partial}{\partial\alpha_u^\dagger}\frac{\partial}{\partial\alpha_u^\dagger}\right\}\alpha_s^\dagger\alpha_i^\dagger.\end{aligned} \tag{26}$$

Now we organise the terms. Collecting the first derivative terms, which are deterministic 'drift' terms, results in

$$\begin{aligned}&-\frac{\partial}{\partial\alpha_u}\left[2\chi\alpha_u^\dagger\alpha_s\alpha_i\right] - \frac{\partial}{\partial\alpha_u^\dagger}\left[2\chi^*\alpha_u\alpha_s^\dagger\alpha_i^\dagger\right] \\ &+\frac{\partial}{\partial\alpha_s}\left[\chi^*\alpha_u\alpha_u\alpha_i^\dagger\right] + \frac{\partial}{\partial\alpha_s^\dagger}\left[\chi\alpha_u^\dagger\alpha_u^\dagger\alpha_i\right] \\ &+\frac{\partial}{\partial\alpha_i}\left[\chi^*\alpha_u\alpha_u\alpha_s^\dagger\right] + \frac{\partial}{\partial\alpha_i^\dagger}\left[\chi\alpha_u^\dagger\alpha_u^\dagger\alpha_s\right].\end{aligned} \tag{27}$$

These can be immediately converted into SDE drift terms where the leading derivative supplies the 'which field' information and the argument (in square brackets '$[\cdots]$') supplies the change in that field.

Collecting the second derivative terms, which are noise-like diffusion terms, results in

$$-\frac{1}{2}\frac{\partial}{\partial\alpha_u}\frac{\partial}{\partial\alpha_u}\{2\chi\alpha_s\alpha_i\}-\frac{1}{2}\frac{\partial}{\partial\alpha_u^\dagger}\frac{\partial}{\partial\alpha_u^\dagger}\left\{2\chi^*\alpha_s^\dagger\alpha_i^\dagger\right\}$$
$$+\frac{1}{2}\frac{\partial}{\partial\alpha_s}\frac{\partial}{\partial\alpha_i}\{2\chi^*\alpha_u\alpha_u\}+\frac{1}{2}\frac{\partial}{\partial\alpha_s^\dagger}\frac{\partial}{\partial\alpha_i^\dagger}\{2\chi\alpha_u^\dagger\alpha_u^\dagger\}. \tag{28}$$

These inform us as to the noise terms and their correlations that will appear in a SDE equivalent picture; the noise amplitudes being the square root of the argument in braces.

These Fokker–Planck equation terms can be converted into temporal SDEs using standard techniques [37–39], and by then transforming them into a co-moving frame [34], we can arrive at the set of spatially propagated SDE's (2)–(7) used in the simulation model. Although reasonable in the case of weak dispersion, as is the case here, in general the conversion of a material's dispersive response between the temporally propagated and spatially propagated domains is not straightforward [48, 49].

Appendix B. Nonlinearity and power

A key feature of the degenerate-pump FWM nonlinear interaction used in our simulations is that it produces pairs of entangled signal and idler fields (photons). It shares this property with the more commonly used second order parametric nonlinearity [39] (usually denoted $\chi^{(2)}$), which generates the same kind of entangled pairs but from single pump photons, not pairs. Although this difference is not trivial, the SDE equations for a $\chi^{(2)}$ nonlinearity are similar in form, although with no quantum noise term applied to the pump field. To test what differences might appear between the two models, some simulations were also done with this $\chi^{(2)}$ model and system parameters rescaled to match the nonlinear effects; the results were remarkably similar in character, indicating that our conclusions are not specific to the FWM model we present here. In both cases we take the usual approach in that the nonlinear response is treated as instantaneous. This is a reasonable approximation since typical nonlinear response times in dielectrics are of the order of femtoseconds or less [50].

In these pair-producing nonlinear interactions, higher pump powers lead to larger amplitudes for the signal and idler fields. Even though our hybrid simulation strategy described in an earlier appendix considerably reduces sampling error, it nevertheless cannot overcome sampling difficulties if the fields produced are too weak. Thus, as stated in the text, we have to run the simulations at a much higher pump power than present in our nominal experimental target [29], just so as to get good simulation statistics (i.e. at least $\sim 10^6$ higher). This means that we rely on the scaling behaviour of the FWM terms in (2) to (5), the weakness of the nonlinearity, and the simulation's lack of any SPM term to nevertheless still give representative results.

However, it is important to remember that we are not here attempting some exact simulation of a QNI experiment based on Pearce *et al* [29], but instead we are using it as a representative scheme to test the generation and recovery of entanglement information under the influence of material dispersion. As a result, the specific pump power used is not of direct relevance to our conclusions regarding the recovery of useful entanglement information as a result of the time-averaging at the detector.

Appendix C. A toy model of entanglement recovery

A toy model of correlation recovery by averaging is possible, although perhaps it is too simple: in our QNI description, correlated quantities are complex valued, accumulated gradually, and undergo phase shifts before being overlaid on one another again and again, all with differing time shifts. In this toy model, the quantities are real valued and we impose only a simple time shift.

Generate a time-series of uncorrelated, zero-average, random numbers A, and make a copy C, but with a time index offset so that for all indices j, we have

$$A_j = C_{j+1}. \tag{29}$$

There are no correlations between the time-synchronised elements since $\langle A_j C_j\rangle = \langle A_j A_{j+1}\rangle = 0$, and on this basis the two time-series' appear uncorrelated. However, now take simple time-averages of A and C, to make two new series B and D, where

$$B_j = \frac{1}{2}\left(A_j + A_{j+1}\right) \tag{30}$$

$$\text{and} \quad D_j = \frac{1}{2}\left(C_j + C_{j+1}\right). \tag{31}$$

But since we also know that D can be expressed in terms of A, we can also write

$$D_j = \frac{1}{2}\left(A_{j-1} + A_j\right) \tag{32}$$

we see that between the time-synchronised elements of B and D there *are* correlations, i.e.

$$\left\langle B_j D_j \right\rangle = \frac{1}{4}\left\langle A_j^2 \right\rangle. \tag{33}$$

Thus we see that time averaging provides us visible time-synchronised correlations that can be tracked back to A and C, despite there being none visible without it.

ORCID iDs

Paul Kinsler https://orcid.org/0000-0001-5744-8146
Martin W McCall https://orcid.org/0000-0003-0643-7169
Rupert F Oulton https://orcid.org/0000-0002-5070-3623
Alex S Clark https://orcid.org/0000-0002-9161-3667

References

[1] Aubrun G, Lami L, Palazuelos C and Plávala M 2022 Entanglement and superposition are equivalent concepts in any physical theory *Phys. Rev. Lett.* **128** 160402
[2] Zou X Y, Wang L J and Mandel L 1991 Induced coherence and indistinguishability in optical interference *Phys. Rev. Lett.* **67** 318
[3] Wang L J, Zou X Y and Mandel L 1991 Induced coherence without induced emission *Phys. Rev.* A **44** 4614
[4] Wiseman H M and Mølmer K 2000 Induced coherence with and without induced emission *Phys. Lett.* A **270** 245
[5] Viswanathan B, Lemos G B and Lahiri M 2021 Resolution limit in quantum imaging with undetected photons using position correlations *Opt. Express* **29** 38185
[6] Fuenzalida J, Hochrainer A, Lemos G B, Ortega E, Lapkiewicz R, Lahiri M and Zeilinger A 2022 Resolution of quantum imaging with undetected photons *Quantum* **6** 646
[7] Lahiri M, Hochrainer A, Lapkiewicz R, Lemos G B and Zeilinger A 2019 Nonclassicality of induced coherence without induced emission *Phys. Rev.* A **100** 053839
[8] Moreau P-A, Toninelli E, Gregory T and Padgett M J 2019 Imaging with quantum states of light *Nat. Rev. Phys.* **1** 367
[9] Padgett M J and Boyd R W 2017 An introduction to ghost imaging: quantum and classical *Phil. Trans. R. Soc.* A **375** 20160233
[10] Basset M G, Setzpfandt F, Steinlechner F, Beckert E, Pertsch T and Gräfe M 2019 Perspectives for applications of quantum imaging *Laser Photon. Rev.* **13** 1900097
[11] Chekhova M V and Ou Z Y 2016 Nonlinear interferometers in quantum optics *Adv. Opt. Photon.* **8** 104
[12] Kolobov M I (ed) 2007 *Quantum Imaging* 1st edn (Berlin: Springer) p 316
[13] Yang T-H, Zhang C-N, Dou J-P, Pang X-L, Li H, Zhou W-H, Chang Y-J and Jin X-M 2021 Time-bin entanglement built in room-temperature quantum memory *Phys. Rev.* A **103** 062403
[14] Aumann P, Prilmüller M, Kappe F, Ostermann L, Dalacu D, Poole P J, Ritsch H, Lechner W and Weihs G 2022 Demonstration and modeling of time-bin entangled photons from a quantum dot in a nanowire *AIP Adv.* **12** 055115
[15] De S, Gil-Lopez J, Brecht B, Silberhorn C, Sanchez-Soto L L, Hradil Z and Rehacek J 2021 Effects of coherence on temporal resolution *Phys. Rev. Res.* **3** 033082
[16] Tran Q H and Nakajima K 2021 Learning temporal quantum tomography *Phys. Rev. Lett.* **127** 260401
[17] Castellani L 2021 Entropy of temporal entanglement (arXiv:2104.05722)
[18] Marcikic I, de Riedmatten H, Tittel W, Zbinden H, Legré M and Gisin N 2004 Distribution of time-bin entangled qubits over 50 km of optical fiber *Phys. Rev. Lett.* **93** 180502
[19] Inagaki T, Matsuda N, Tadanaga O, Asobe M and Takesue H 2013 Entanglement distribution over 300 km of fiber *Opt. Express* **21** 23241
[20] Yu Y *et al* 2020 Entanglement of two quantum memories via fibres over dozens of kilometres *Nature* **578** 240
[21] Pirandola S, Laurenza R, Ottaviani C and Banchi L 2017 Fundamental limits of repeaterless quantum communications *Nat. Commun.* **8** 15043
[22] Zwerger M, Pirker A, Dunjko V, Briegel H J and Dür W 2018 Long-range big quantum-data transmission *Phys. Rev. Lett.* **120** 030503
[23] Khatri S, Matyas C T, Siddiqui A U and Dowling J P 2019 Practical figures of merit and thresholds for entanglement distribution in quantum networks *Phys. Rev. Res.* **1** 023032
[24] Pittman T B, Shih Y H, Strekalov D V and Sergienko A V 1995 Optical imaging by means of two-photon quantum entanglement *Phys. Rev.* A **52** R3429
[25] Erkmen B I and Shapiro J H 2010 Ghost imaging: from quantum to classical to computational *Adv. Opt. Photon.* **2** 405
[26] Shirai T, Setälä T and Friberg A T 2010 Temporal ghost imaging with classical non-stationary pulsed light *J. Opt. Soc. Am.* B **27** 2549
[27] Ryczkowski P, Barbier M, Friberg A T, Dudley J M and Genty G 2016 Ghost imaging in the time domain *Nat. Photon.* **10** 167
[28] Kolobov M I, Giese E, Lemieux S, Fickler R and Boyd R W 2017 Controlling induced coherence for quantum imaging *J. Opt.* **19** 054003
[29] Pearce E, Phillips C C, Oulton R F and Clark A S 2020 Heralded spectroscopy with a fiber photon-pair source *Appl. Phys. Lett.* **117** 054002

[30] Hillery M and Zubiary M S 2006 Entanglement conditions for two-mode states *Phys. Rev. Lett.* **96** 050503
[31] Drummond P D and Carter S J 1987 Quantum-field theory of squeezing in solitons *J. Opt. Soc. Am.* B **4** 1565
[32] Carter S J, Drummond P D, Reid M D and Shelby R M 1987 Squeezing of quantum solitons *Phys. Rev. Lett.* **58** 1841
[33] Carter S J 1993 The Raman modified nonlinear Schrödinger equation *PhD Thesis* University of Queensland
[34] Carter S J 1995 Quantum theory of nonlinear fiber optics: phase-space representations *Phys. Rev.* A **51** 3274
[35] Corney J F, Heersink J, Dong R, Josse V, Drummond P D, Leuchs G and Andersen U L 2008 Simulations and experiments on polarization squeezing in optical fiber *Phys. Rev.* A **78** 023831
[36] Werner M J and Drummond P D 1993 Simulton solutions for the parametric amplifier *J. Opt. Soc. Am.* B **10** 2390
[37] Drummond P D and Gardiner C W 1980 Generalised P-representations in quantum optics *J. Phys. A: Math. Gen.* **13** 2353
[38] Gardiner C W 2004 *Handbook of Stochastic Methods Springer Series in Synergetics* vol 13 3rd edn (Berlin: Springer) p 415
[39] Drummond P D and Hillery M 2014 *Quantum Theory of Nonlinear Optics* (Cambridge: Cambridge University Press) p 380
[40] Smith B J and Raymer M G 2007 Photon wave functions, wave-packet quantization of light, and coherence theory *New J. Phys.* **9** 414
[41] Titulaer U M and Glauber R J 1966 Density operators for coherent fields *Phys. Rev.* **145** 1041
[42] Kinsler P and Drummond P D 1991 Quantum dynamics of the parametric oscillator *Phys. Rev.* A **43** 6194
[43] Kinsler P and Drummond P D 1991 Comment on 'Langevin equation for the squeezing of light by means of a parametric oscillator' *Phys. Rev.* A **44** 7848
[44] Kinsler P 1996 Testing quantum mechanics using third-order correlations *Phys. Rev.* A **53** 2000
[45] Hyllus P, Gühne O, Bruß D and Lewenstein M 2005 Relations between entanglement witnesses and Bell inequalities *Phys. Rev.* A **72** 012321
[46] Kinsler P and New G H C 2005 Wideband pulse propagation: single-field and multi-field approaches to Raman interactions *Phys. Rev.* A **72** 033804
[47] Walls D F 1983 Squeezed states of light *Nature* **306** 141
[48] Kinsler P 2018 Uni-directional optical pulses, temporal propagation, and spatial and temporal dispersion *J. Opt.* **20** 025502
[49] Kinsler P 2018 A comparison of the factorization approach to temporal and spatial propagation in the case of some acoustic waves *J. Phys. Commun.* **2** 025011
[50] Das S K *et al* 2013 First measurement of the non-instantaneous response time of a $\chi^{(3)}$ nonlinear optical effect *EPJ Web Conf.* **41** 12005